electronics

MDPI

Article

Magnetic Design Aspects of Coupled-Inductor Topologies for Transient Suppression

Sadeeshvara Silva Thotabaddadurage [1,*], Nihal Kularatna [2] and D. Alistair Steyn-Ross [2]

[1] Electric Power Engineering Centre, University of Canterbury, Christchurch 8140, New Zealand
[2] School of Engineering, University of Waikato, Hamilton 3240, New Zealand
* Correspondence: sadeesh.silva@canterbury.ac.nz or sadeeshvara.udayanga@gmail.com

Abstract: Based on the discovery of the surge absorption capability of supercapacitors, a transient protector named supercapacitor-assisted surge absorber (SCASA) was designed and implemented in a commercial device. Despite its simplicity, the circuit topology consisted of a coupled inductor wound around a specially selected magnetic core. This paper elucidates the design aspects of SCASA coupled-inductor topologies with a special focus on the magnetic action of core windings during transient propagation. The non-ideal operation of the SCASA transformer was studied based on a semi-empirical approach with predictions made by using magnetizing and leakage permeances. The toroidal flux distribution through the transformer was also determined for a 6 kV/3 kA combinational surge, and these findings were validated by using a lightning surge simulator. In predicting the possible effects of magnetic saturation, the hysteresis properties of different powdered-iron and ferrite core types were considered to select the optimal design for surge absorption. The test results presented in this research revealed that X-Flux powdered-iron toroid and air-gapped EER ferrite yielded exceptional performance with ∼10% and ∼20% lower load–voltage clamping compared to that of the existing Kool μu design. These prototypes further demonstrated a remarkable surge endurance, withstanding over 250 consecutive transients. This paper also covers details of three-winding design optimizations of SCASA and LTSpice simulations under the IEC 61000/IEEE C62.45 standard transient conditions.

Keywords: supercapacitors; transient absorption; magnetic permeance; coupled inductor; transformer modeling; LTSpice simulations; powdered iron; ferrites

Citation: Silva Thotabaddadurage, S.; Kularatna, N.; Steyn-Ross, D.A. Magnetic Design Aspects of Coupled-Inductor Topologies for Transient Suppression. *Electronics* **2023**, *12*, 246. https://doi.org/10.3390/electronics12010246

Academic Editor: Cao Guan

Received: 17 October 2022
Revised: 26 December 2022
Accepted: 27 December 2022
Published: 3 January 2023

1. Introduction

1.1. Power Quality Issues and Vulnerabilities of Modern Electronics

Power-line voltage disturbances downgrade the quality of utility mains. In general, AC power transmission occurs at an ostensible RMS voltage under a percentage tolerance of ±6–10% [1], and single- or three-phase mains are often subject to power quality issues. RMS fluctuations, such as sags and over-voltages, transients, noise, and harmonics, are among the typical voltage disturbances (see Figure 1) caused by lightning, inductive switching, heavy loads, etc. Of the different power quality problems, transient phenomena cause the greatest damage to a critical load if not appropriately controlled [2]. Thus, this research presents the magnetic design details of coupled-inductor-based transient protectors designed using various powdered iron and ferrite core types. Transient-surge protector devices (SPDs) are designed to absorb and dissipate the transient energy while continually facilitating the flow of mains electricity to the load. Every design prototype discussed in this paper was first tested under a 50 Hz mains frequency prior to the validation of the transient absorption capability.

The main objective of this study was to analyze the commercial SCASA protector by using permeance theory and predict its transformer's action under 6 kV, 3 kA combinational surge conditions. Compared to the existing design, this research elucidates topological

advancements by using a three-winding magnetic core and compares the performance levels of various powdered-iron- and ferrite-based prototypes. While suppressing transient propagation, the new prototypes revealed superior load protection with up to 20% reduction in the clamping voltage. Moreover, improvements in the maximum surge endurance are also discussed by using the UL-1449 test protocols. Air-gapped EER ferrite and an X-Flux powdered core manifested the best transient immunity, withstanding over 250 combined surges. Next, we present the principles of SPD design and combinational transient test waveforms applied to IEC/IEEE standards.

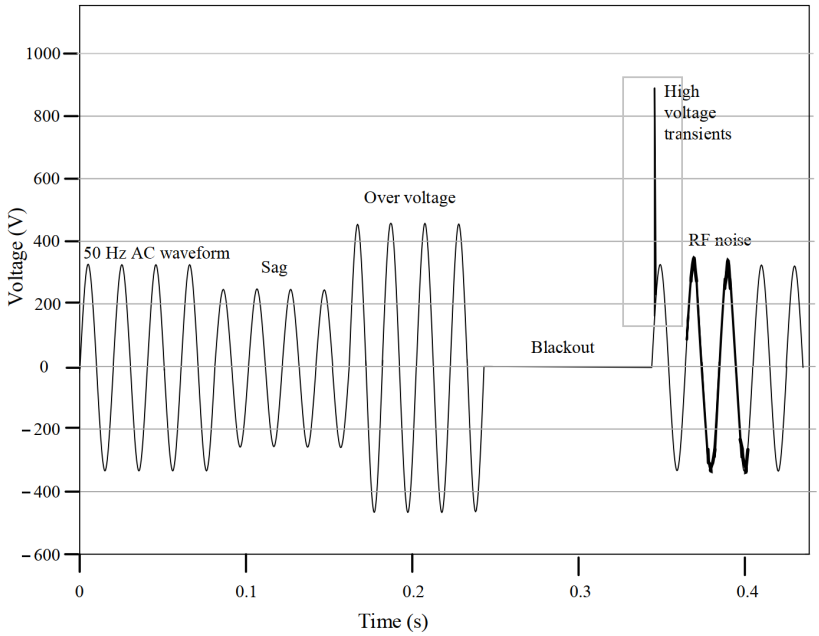

Figure 1. Voltage fluctuations on a 230 V RMS, 50 Hz utility mains supply.

1.2. Fundamental Concepts of Surge Protection

In general, all SPDs work on the concept of impedance dividers; thus, they follow the voltage division principle to eliminate the voltage stress of a transient surge [3]. To exemplify the operation of a basic surge protector, in Figure 2a, an AC supply (v_{supply}), non-linear shunt device with impedance Z_{NLD}, and a surge occurrence (v_{surge}) are considered. The series impedance Z_{series} shown in Figure 2a can be due to the ohmic resistance of the connection cables, inductive reactance ($X_L = \omega L$) of a coil in series, and/or the complex impedance of the transmission line [4]. v_{surge}, which is superimposed on a power line, shares part of its magnitude across Z_{series}, whereas the remaining surge voltage appears across Z_{NLD}. In contrary to the series inductive impedance, which increases with high-frequency transients, Z_{NLD} decreases at frequencies of the kHz–MHz order, diverting the surge away from the load [5]. Nonlinear devices (NLDs), such as metal oxide varistors (MOVs), bidirectional break-over diodes (BBDs), gas discharge tubes (GDTs), capacitors (Cs), and thyristors (THYs), are widely used in SPD design. Notably, these NLDs, which enter into the low-impedance conduction mode under transients, dissipate excessive transient energy while maintaining a safe voltage (V_{NLD}) across the load. As per the voltage division, V_{NLD} can be expressed as:

$$V_{NLD} = \frac{Z_{NLD}}{Z_{NLD+Z_{series}}} \quad (1)$$

Equation (1) proves how increased Z_{series} and reduced Z_{NLD} result in a lower V_{NLD}, thus minimizing the voltage stress on the critical load. Figure 2b demonstrates a combined SPD circuit with a GDT, two inductors (Z_{series_1} and Z_{series_2}), an MOV, and a BBD placed along the path of a 10 kV transient superimposed on 230 V, 50 Hz mains. The series

inductors in this case help to reduce the voltage magnitude, whereas the GDT, and MOV divert the high transient current while safely clamping the voltage. Moreover, a BBD with a superior reaction time provides effective clamping at the load end, thus preventing any EMI issues. By complementing the characteristics of different protective components, the combined SPD circuit performs satisfactorily, as depicted in Figure 2b. Since a single surge protector may not ideally carry all components due to cost constraints, in Section 2, we present an overview of a supercapacitor-based surge protector with a reduced number of components.

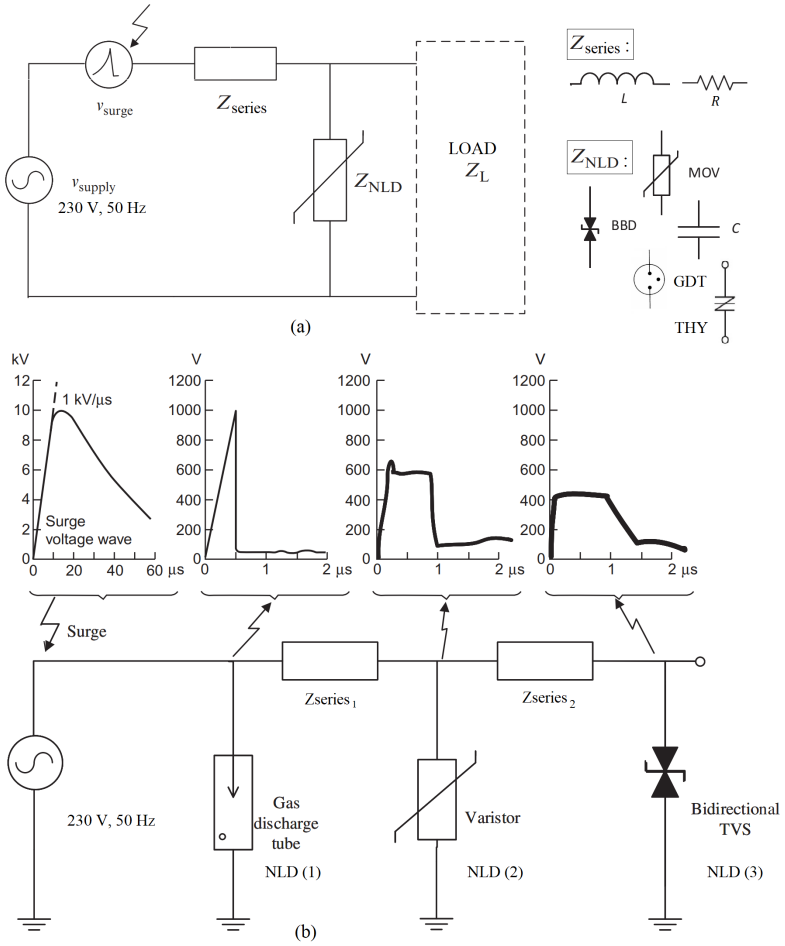

Figure 2. Principle of voltage division applied to surge protector design: (**a**) simplified circuit diagram of load in connection with a basic shunt NLD; (**b**) common series and shunt protection devices [6].

1.3. Standard Surge Waveforms: 1.2/50 µs Open-Circuit Voltage Wave and 8/20 µs Short-Circuit Current Wave

For testing SPD devices, standard surge waveforms are recommended by the IEC 61000-4-5 and ANSI/IEEE C62.45 test standards [1,7]. The widely used 1.2/50–8/20 µs combinational wave is a combination of two waves: a 1.2/50 µs open-circuit voltage wave and a 8/20 µs short-circuit current wave.

According to the test standard, the open-circuit voltage waveform (Figure 3a,b) has the following characteristics:

— Front time/rise time (T_r): 1.2 µs ± 0.36 µs;

— Duration (T): 50 µs ± 10 µs.

The rise time of the voltage waveform is found by using $T_r = 1.67 \times t_1$, where t_1 is the time gap between 90% and 30% of the voltage magnitudes on the rising edge ($t_1 = t_{90} - t_{30}$). Furthermore, the time gap T of the wave is considered as the interval between the virtual

origin and 50% of the voltage magnitude on the falling half. The virtual origin of the wave is taken as the point where the gradient line between the 90% and 30% amplitude points (rising edge) intersects with the voltage zero axis. The definition for this waveform comes with its characteristics: 1.2 µs rise time and 50 µs duration; thus, it is named the 1.2/50 µs combination voltage wave.

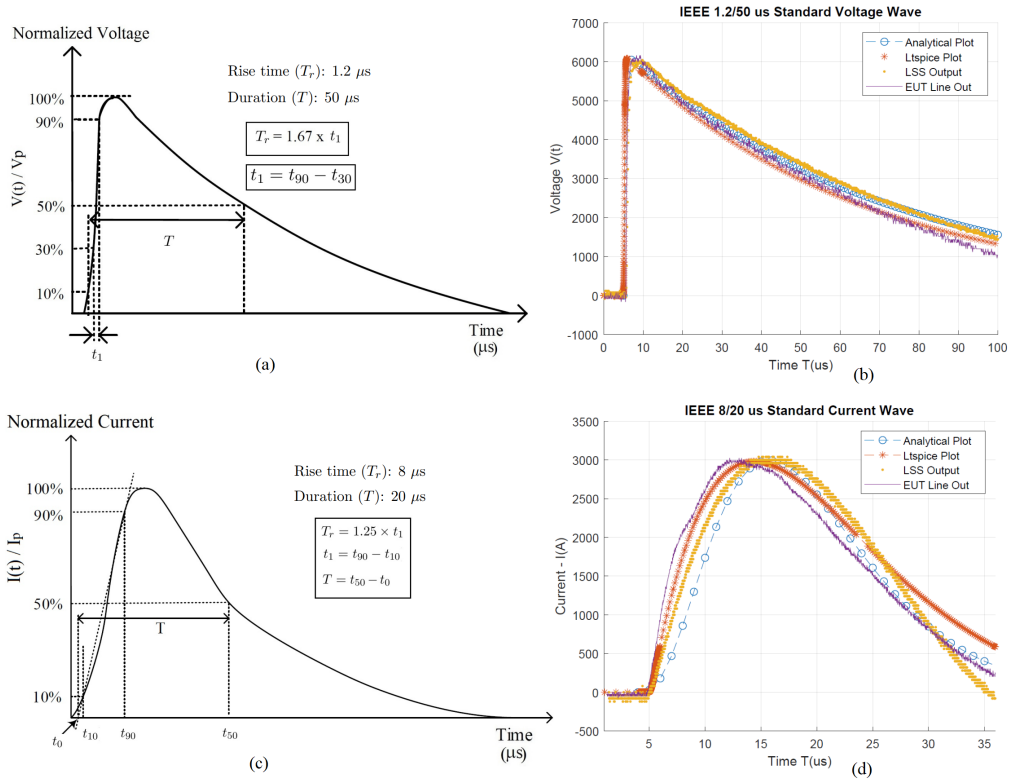

Figure 3. The 1.2/50 µs voltage waveform and 8/20 µs combined current waveform: (**a**) nominal waveform of the 1.2/50 µs voltage wave as per IEEE C62.41; (**b**) comparison plots for a 6 kV 1.2/50 µs voltage wave: analytical plot, LTSpice plot, LSS output, and EUT line out; (**c**) nominal waveform of the 8/20 µs current wave as per IEEE C62.41; (**d**) comparison plots for a 3 kA 8/20 µs current wave: analytical plot, Ltspice plot, LSS output, and EUT line out.

The combination current waveform is produced when the 1.2/50 µs voltage wave is short-circuited [7], and the resulting short-circuit current (Figures 3c,d) has the following characteristics:

— Front time/rise time (T_r): 8 µs (+1.0, –2.5) µs;

— Duration (T): 20 µs (+8, –4) µs.

The rise time of the current waveform is found according to $T_r = 1.25 \times t_1$, where t_1 is the time gap between 90% and 10% of the current magnitudes on the rising edge of the waveform ($t_1 = t_{90} - t_{10}$). Moreover, the time gap T of the wave is considered as the interval between the virtual origin (t_0) and 50% (t_{50}) of the current magnitude on the falling edge. The virtual origin of the wave is taken as the point where the gradient line between 90% and 10% magnitudes on the rising half intersects with the current zero axis. The time gap $T = t_{50} - t_0$ of this current waveform equals 20 µs. The definition for this wave comes with its characteristics: 8 µs rise time and the 20 µs duration; hence, it is named the 8/20 µs combination current wave.

While two of these combined voltage/current waveforms stipulate suitable models for lighting surges, their wave shapes can deviate due to the internal impedances of surge simulators and path impedances that arise due to resistive, capacitive, and inductive circuit elements [8,9]. Therefore, to comprehend the deviation of an open-circuit voltage wave and

short-circuit current wave, we compare the analytical, experimental, and numerical waveforms illustrated in Figure 3b,d. The analytical plots for the voltage/current waveforms were based on the mathematical representations found in IEC 61000 and IEEE C62.45 [7]; the numerical LTSpice plots were obtained from the simulation circuit shown in Figure 13. Moreover, the experimental waveforms were drawn from Lightning Surge Simulator (LSS) output data and Equipment Under Test (EUT) line data.

1.4. Supercapacitors' Surge-Withstanding Capabilities

Supercapacitors (SCs) have much larger capacitances than those of electrolytic capacitors (ECs); thus, SCs can store greater levels of energy than ECs with the same canister volume [10]. In Figure 4c, we present a comparison of the maximum energy storage ($0.5\ CV^2$) for comparable canister sizes of SCs and ECs. However, the DC voltage ratings of all supercapacitor types are fairly low, typically a few volts: 2–4 V [11]. Notably, due to their larger capacitances, SCs have an expanded charging curve (with a greater time constant) compared to those of ECs, as demonstrated in Figure 4a. For example, when combined with a 1 ohm charging-loop resistance, a 100 µF capacitor will reach its full voltage (DC supply source) within just 0.5 milliseconds. However, a supercapacitor of 1 F will take about 5 s for a similar circuit loop. If a DC voltage supply appears for only 10 µs in the form of a voltage step (see Figure 4a), an SC will not develop a considerable voltage, while the loop resistance will circumvent a huge share of energy in terms of surge dissipation.

Figure 4d presents how voltage build-up occurs across SCs and ECs for a 6 kV, 1.2/50 µs transient pulse. In all cases, it is seen that ECs develop several thousands of volts under the 6 kV transient, whereas 1, 25, and 100 F SCs are charged up to few millivolts. With this expanded nature of SC charging, it is found that the voltage development v_{sc} is substantially smaller than the v_c of a normal EC capacitor ($v_{sc} << v_c$). Notably, v_{sc} is smaller than the DC voltage rating of a supercapacitor, thus eliminating any chances of failure when subjected to a transient surge. Contrarily, ECs demonstrate signs of degradation by developing bulging tops, as verified in surge tests (see Figure 4a), leading to physical damage of the devices. More details about supercapacitors' transient behavior and surge dissipation in SCs' RC-circuit loops can be found in [12]. In Section 2, we present an overview of how an SC can be placed in a practical surge protector to provide improved performance.

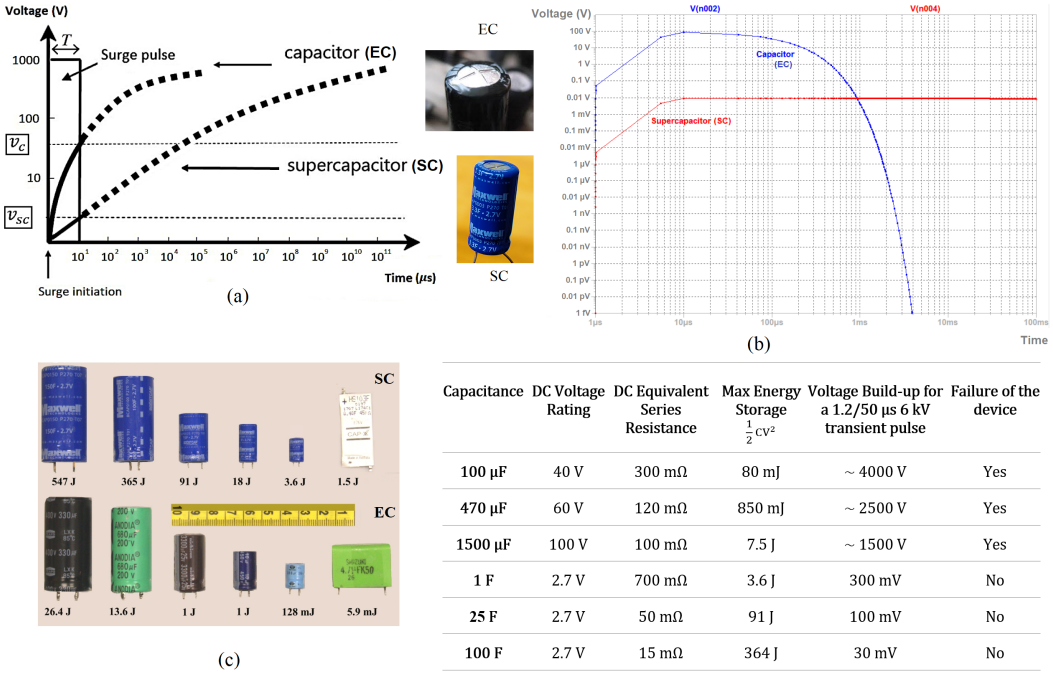

Capacitance	DC Voltage Rating	DC Equivalent Series Resistance	Max Energy Storage $\frac{1}{2}CV^2$	Voltage Build-up for a 1.2/50 μs 6 kV transient pulse	Failure of the device
100 μF	40 V	300 mΩ	80 mJ	~ 4000 V	Yes
470 μF	60 V	120 mΩ	850 mJ	~ 2500 V	Yes
1500 μF	100 V	100 mΩ	7.5 J	~ 1500 V	Yes
1 F	2.7 V	700 mΩ	3.6 J	300 mV	No
25 F	2.7 V	50 mΩ	91 J	100 mV	No
100 F	2.7 V	15 mΩ	364 J	30 mV	No

(d)

Figure 4. Comparison of supercapacitor and capacitor characteristics: (**a**) voltage build-up for SCs and ECs for a 1000 V, 10 μs step transient; (**b**) simulated voltage development for a 1 F SC and 100 μF EC for a 1000 V, 10 μs step pulse; (**c**) energy storage capabilities of SCs vs. ECs with similar canister sizes [13]; (**d**) DC voltage rating, ESR, energy storage comparison of SCs vs. ECs and the voltage build-up for a 1.2/50 μs, 6 kV transient.

2. Overview of the SCASA Circuit Design

2.1. Topological Features

The empirical validation of the surge absorption potential of supercapacitors resulted in the development of a supercapacitor-based transient suppressor named SCASA. The original circuit design comprised an SC sub-circuit, as shown in Figure 5b. The low DC rating (2–4 V) of SCs prevents their direct application across 230 V AC mains (or SCs cannot be placed in parallel with an NLD) [14]. Thus, in designing the SCASA topology, coupled inductor windings were utilized with a powdered iron magnetic core (Kool μu 0077071A7-Magnetics Inc.), which had a relative permeability of μ_r = 60 [15]. In the SCASA design depicted in Figure 5b, a configuration of two coupled windings was selected in such way that the primary coil (N_1 = 6 turns) created a reduced-impedance path for transient propagation in comparison with the more inductive secondary, which consisted of 28 turns (N_2). Overall, magnetic induction of the two SCASA coils minimized the passage of transient energy to the load in terms of surge flux storage within the toroid. The topology also facilitated the continuous flow of 230 V, 50 Hz mains without blocking the AC line frequency.

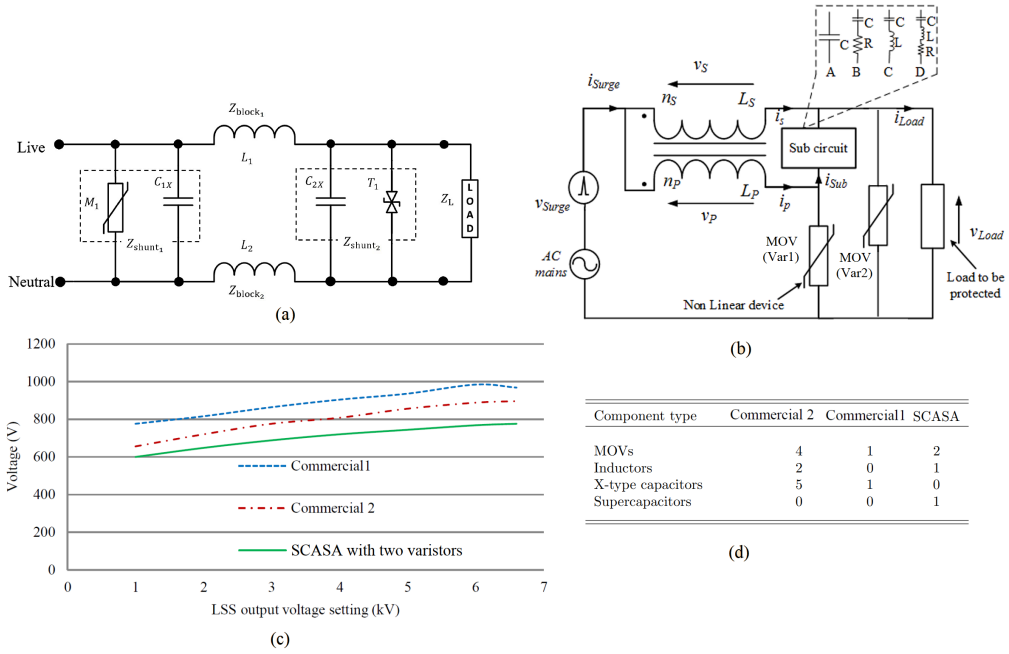

Component type	Commercial 2	Commercial1	SCASA
MOVs	4	1	2
Inductors	2	0	1
X-type capacitors	5	1	0
Supercapacitors	0	0	1

Figure 5. Comparison of the SCASA topology with other commercial SPDs: (**a**) traditional differential-mode surge protector; (**b**) generalized SCASA circuit; (**c**) load–voltage comparison of SCASA and other commercial protectors; (**d**) component count comparison of SCASA and other commercial surge protectors.

As mentioned previously, the novelty in the SCASA design is the addition of a supercapacitor sub-circuit. Out of the various sub-circuit combinations (A, B, C, and D in Figure 5b), it was validated that the most effective combination was B (*RC*) [13]. Therefore, in a practical SCASA protector circuit, a 5 F SC and a 1 Ω high-power resistor were placed between the ends of two coupled-inductor coils to make sure that the DC-rated voltage of the SC was not exceeded. In addition, the two nonlinear MOVs (Var 1 and Var 2) dissipated excess transient energy while a safer clamping level was maintained at the load end. Figure 5c demonstrates how the SCASA clamping voltage varied for a range of surge settings (1–6 kV) and provides comparisons with two other industrial SPDs. As a commercially successful design, the SCASA transient protector competes well with other commercial SPDs due to its low component count (see Figure 5d) and superior performance. The magnetic design aspects of the coupled inductor will be investigated next.

2.2. Powdered-Iron vs. Ferrite Magnetic Cores

When the SCASA circuit design was first implemented, special considerations were made to select a suitable magnetic core. According to the initial investigations, it was revealed that only a powdered-iron core had satisfactory performance, whereas commercial ferrites failed to absorb an adequate level of surge. In the present SMART-TViQ design, a powdered-iron toroid is utilized, as illustrated in Figure 6a (Kool μu toroid, Magnetics, Inc., Pittsburgh, PA, USA). This core has a relative permeability μ_r = 60 [16]. Contrary to high-permeability (μ_r = 10,000) ferrite cores (Figure 6b) [17], powdered materials are fabricated with distributed air-gaps, resulting a permeability reduction. Notably, this air-gapping effect in powdered cores provides a greater energy storage capability to the core than that of pure ferrites [18]. To investigate this further, we designed tests to observe the magnetic operation of the SCASA coupled-transformer coils (more details found in Section 3.2).

Figure 6. Comparison of magnetic properties: (**a**) Kool μu powdered-iron toroid (0077071A7); (**b**) W-Ferrite toroid (ZW43615TC).

In addition to the Kool μu core's high energy storage, it had a relatively high level of magnetic saturation (10,500 gauss/1.05 T) compared to that of the W-ferrite core, which saturated at 3900 gauss/3.9 T (Table 1) [17]. To study the suitability of these materials, we determined the peak toroidal flux density induced due to a 3 kA transient, as described in Section 3.5. Having a low magnetic saturation is another drawback that limits ferrites' application in surge protection circuits. However, the saturation level can be elevated when an air gap is introduced to a ferrite body; Section 2.3 describes the benefits of the air gapping of toroids. Moreover, due to reduced core losses (550 mW/cm^3), the Kool μu core is applicable in transient conditions, as well as 230 V AC, without substantial core/heat losses [19]. However, when designing high-performance SCASA prototypes, we experimented with various other powdered-iron cores, such as High-Flux and X-Flux toroids. The characteristics of the hysteresis behaviors of all powdered materials and other ferrites used in designing prototypes are illustrated below (Figure 7 and Table 1). Compared to the low saturation levels of ferrites, both X-Flux and High-Flux cores possessed superior saturation flux densities of 15,000 gauss (1.5 T) and 16,000 gauss (1.6 T), respectively. In Section 4, we present the experimental results obtained for different SCASA prototypes designed by using various magnetic core samples and compare their performance with that of the existing Kool μu design.

Table 1. Comparison of the magnetic properties of various powdered-iron and ferrite materials used to design SCASA prototypes [17,19].

Magnetics Material	Material Composition	Initial Relative Permeability (μ_r)	Saturation Flux Density (Gauss)	Coercive Force H_c (Oersteds) 50% μ_r	Core Loss @100 kHz (mW/cm^3)
Kool mu	Al, Si, Fe	14-125	10,500	100	550
High Flux	Fe, Ni	14-160	15,000	185	625
X Flux	Fe, Si	19-125	15,000	170	1280
W Ferrite	Fe, Mn, Zn	10,000	3900	0.15	–
J Ferrite	Fe, Mn, Zn	5000	4300	0.2	–
R Ferrite	Fe, Mn, Zn	2300	4700	0.18	~100
P Ferrite	Fe, Mn, Zn	2500	4700	0.18	~100

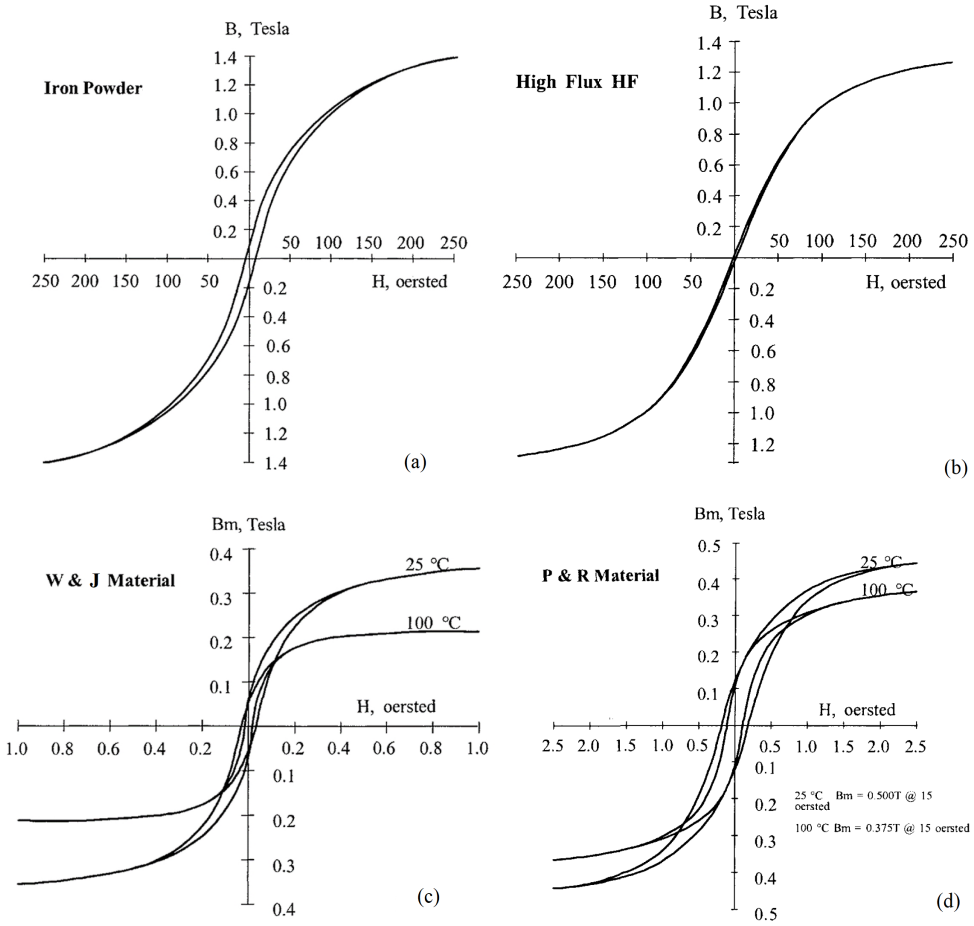

Figure 7. Hysteresis characteristics comparison of powdered-iron and ferrite materials used to design SCASA prototypes: (**a**) Kool μu (powdered iron) hysteresis loop; (**b**) High-Flux (powdered iron) hysteresis loop; (**c**) hysteresis behavior of W and J ferrites; (**d**) hysteresis behavior of P and R ferrites [20].

2.3. Significance of the Air Gapping of a Ferrite Core

Since the soft ferrite materials described above (W, J, R, and P ferrites) possess high relative permeabilities (narrow hysteresis loop) and low magnetic saturation levels, we discovered that these materials were not suited for surge protector design. In addition, due to the low energy storage capabilities of soft ferrites, these performed poorly when tested with the SCASA prototypes. Therefore, as an alternative approach to utilizing pure ferrite core samples for the SCASA transformer, we conducted experiments using air-gapped ferrites (with comparable properties to those of powdered iron) cores. Our initial investigations involved testing single- and double-gapped toroidal cores based on W-ferrite material. The following calculations justify how the relative permeability (μ_r) can be reduced significantly by adding an air gap to the magnetic path length.

The reduction effect of the magnetic reluctance of a core in the presence of an air gap was explained in [21]; based on our previous analytical work, the effective permeability $\mu_l{}'$ of an air-gapped toroid can be deduced as:

$$\mu_l{}' = l_c \left[\frac{\mu_r}{\mu_r l_g + l_c} \right] \tag{2}$$

Note: l_c = the toroidal circular length, l_g = the air-gap length, and μ_r = the relative permeability of an ungapped toroid.

For a single-air-gapped toroid (Figure 8) with a gap length of $l_g = 2$ mm, $l_c = 100$ mm, and $\mu_r = 10{,}000$, by using Equation (2), we have:

$$\mu_l{}' = 100\,\text{mm}\left[\frac{10{,}000}{10{,}000 \times 2\,\text{mm} + 100\,\text{mm}}\right]$$

$$\mu_l{}' \approx 50$$

Moreover, for a double-gapped toroid (Figure 8), $\mu_l{}'$ can be evaluated as follows:

$$\mu_l{}' = 100\,\text{mm}\left[\frac{10{,}000}{10{,}000 \times 4\,\text{mm} + 100\,\text{mm}}\right]$$

$$\mu_l{}' \approx 25$$

These predictions justify that a single air column inside the ferrite yields a substantial drop in the relative permeability (10,000 → 50), whereas a double air column yields a 10,000 → 25 reduction. Our next aim is to compare how the energy storage levels vary for different gapped-core samples.

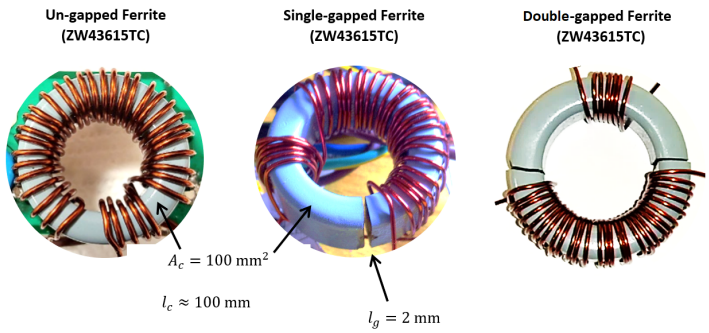

Figure 8. Geometrical configurations of ungapped, single-gapped, and double-gapped ferrites.

According to Ampere's law, the following expression can be derived for the energy $E_\circ$ stored in the air gap, as described in [22].

$$E_\circ = \frac{1}{2}\frac{B^2 v_g}{\mu_\circ} \tag{3}$$

Note: $\vec{B}$ = the magnetic flux density across the toroid, and v_g = the volume of the air gap, as illustrated in Figure 8. The air volume can be determined from $A_c l_g$.

Similarly, we can prove energy stored inside the toroidal core E_c as follows:

$$E_c = \frac{1}{2}\frac{B^2 v_c}{\mu_\circ \mu_r} \tag{4}$$

where v_c is the volume of ungapped toroid given by $A_c l_c$.

Since the toroidal flux during transient excitation uniformly passes through both the core and the air gap, it is possible to establish a proportional relationship to determine $E_\circ / E_c$ as follows:

$$\frac{E_\circ}{E_c} = \frac{\mu_r l_g}{l_c}$$

Importantly, this relationship substantiates that the energy stored inside a single air gap is 200 times greater ($E_\circ = 200 \times E_c$) than the energy retained in an entire ungapped toroid. Furthermore, in the double-gapped core, $E_\circ{}' = 400 \times E_c$. Test results relating to

the transformer inductance properties and clamping improvements of SCASA prototypes based on gapped ferrite toroids are given in Section 4.

2.4. Limitations of the Present Topology and Possible Improvements

The limitations of the present SCASA design can be identified in two forms—the high load–voltage clamping under transients and the high manufacturing cost of the Kool μu powdered core are among the top concerns. To address the first, we developed prototypes with air-gapped ferrites to elevate the surge absorption and dissipate excess transient energy. Apart from the justification of the energy storage capabilities of the gapped ferrites presented above, a detailed discussion about leakage effects and transient losses is given in Section 4.3.

As per the test results observed for the SCASA device under a 6 kV/3 kA combined transient, it was seen that clamped load–voltage lay between 800 and 900 V. However, in Section 1.2, we explained how detrimental effects (internal degradations in load circuits) can arise when voltage clamping increases above 700 V for an extended period. Therefore, we designed SCASA prototypes by using EER-type (based on R-ferrite, R43521A125 Magnetics Inc., Pittsburgh, PA, USA) air-gapped cores to address the above limitation [17]. The new approach yielded better voltage characteristics on the load side with improved transient endurance; more details about this implementation and the related experimental outcomes will be investigated in Section 4.

As an industrially useful surge protector, it is important to have a reduced cost of production for SMART-TViQ devices based on the SCASA technique. However, with the manufacturing complexity (due to distributed air-gaps) of Kool μu powdered toroids, they can be more expensive than gapped ferrites. However, by using mass-produced EER-type cores, a solution to this price constraint was found with an approximate cost reduction of about 40%. Comparisons of the magnetic characteristics of the two core samples and their production costs are given in Section 4.5. In the next section, we examine the magnetics of the SCASA coupled inductor by using a novel theoretical model derived from magnetic permeance.

3. Magnetics of the SCASA Transformer

The use of the Kool μu core for the SCASA coupled inductor introduced various non-ideal transformer characteristics to the core. Unlike a pure ferrite material, where the core reluctance is negligible, the powdered-iron core possessed a high reluctance due to the distributed air gaps [20]. As a consequence, the SCASA coupled inductor wound around the Kool μu toroid showed reduced magnetizing inductance and relatively high leakage inductance. To model these non-ideal properties of the coupled inductor, we developed a magnetic permeance theory, as described below.

3.1. Permeance Model for the Coupled Inductor

In contrast to magnetic permeability (μ_r), which is a characteristic of the material, magnetic permeance Λ is a derived attribute determined by both the permeability and geometry of the core [23,24]. To model the magnetizing inductances of SCASA transformer windings, magnetizing permeance Λ_m was used. By definition, Λ_m is also described as the magnetizing inductance per unit of square turns [24]. Hence, the permeance determines the inductance of a coil due to magnetizing flux. In theory, the links between Λ_m, μ_r, A_c, and l_c are given by (5):

$$\Lambda_m = \frac{\mu_r \mu_o A_c}{l_c} \tag{5}$$

Note: μ_r = the relative permeability and μ_o = the permeability of free space. The formula above substantiates how the magnetizing permeance depends on both the material and geometrical properties of the core. According to industry specifications, Λ_m is known as the

inductance factor A_L. Figure 19 compares the Λ_m values of various powdered-iron and ferrite materials (including gapped ferrites) implemented when designing SCASA prototypes.

To model the leakage inductances of the SCASA transformer, the leakage permeance Λ_σ was used. The practical leakage permeance for toroidal cores is considered proportional to the inner diameter d_{int}. The proportionality factor A is independent of the material and is dependent on how the core is actually wound. The leakage permeance is approximated as:

$$\Lambda_\sigma = A\, d_{int} \tag{6}$$

where $A = 2.3$ μH/m according to empirical estimations [24]. Combining Λ_m and Λ_σ, we can represent the self-inductance of SCASA windings as described below.

The two coupled-inductor coils of the SCASA transformer (Figure 9) possess magnetizing inductances (L_1, L_2) and leakage inductances (l_1, l_2) associated with the primary and secondary sides of the core.

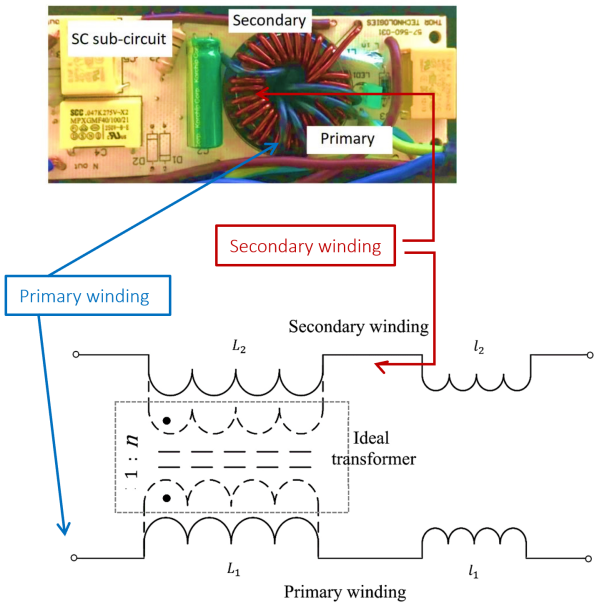

Figure 9. Equivalent circuit of the SCASA transformer.

According to [24], the primary and secondary self-inductances L_p and L_s can be written as:

$$L_p = L_1 + l_1 \tag{7}$$

$$L_s = L_2 + l_2 \tag{8}$$

Incorporating both magnetizing and leakage permeances (Λ_m, Λ_σ) into L_1, L_2 and l_1, l_2, we get:

$$L_1 = \Lambda_m {N_1}^2 \text{ and } l_1 = \Lambda_\sigma {N_1}^2 \tag{9}$$

$$L_2 = \Lambda_m {N_2}^2 \text{ and } l_2 = \Lambda_\sigma {N_2}^2 \tag{10}$$

In designing the SCASA transformer, a greater level of leakage inductance is maintained (due to the distributed air-gap effect of the Kool μu powdered core). In addition, due to the toroidal symmetry of SCASA, it is possible to predict equal sharing of leakage flux between the primary/secondary core windings. Thus, it is assumed that each winding possesses 50% of the leakage permeance ($\Lambda_\sigma/2$) [19,24]. Therefore, by using above permeance Equations (9) and (10), we can express (7), and (8) as:

$$L_p = \Lambda_m {N_1}^2 + \frac{\Lambda_\sigma}{2} {N_1}^2 \tag{11}$$

$$L_s = \Lambda_m {N_2}^2 + \frac{\Lambda_\sigma}{2} {N_2}^2 \tag{12}$$

Furthermore, the magnetic coupling between the two coils, which depends on the mutual inductance (M) of the SCASA core, can be theorized by using Λ_m as per (13).

$$M = \Lambda_m N_1 N_2 \tag{13}$$

In Section 4.3, we present how these inductance properties vary for the Kool μu toroid (Magnetics Inc., Pittsburgh, PA, USA) and compare such measurements for other powdered-iron and ferrite samples adopted in SCASA prototypes. Open-circuit and short-circuit experiments on the coupled inductor were conducted to determine the self-inductances (L_p, L_s) and leakage inductances (l_1, l_2); moreover, series and inverse-series tests were carried out to reveal the mutual inductance M [25].

3.2. Voltage Induction of Primary and Secondary SCASA Windings

Under high-magnitude voltage (1.2/50 μs, 6 kV) and current (8/20 μs, 3 kA) transients, both SCASA MOVs Var 1 and Var 2 exceeded their breakdown limits; thus, they entered into conduction modes [26], as characterized by the appropriate "ON resistances" (R_{ON}) illustrated in Figure 10. The varistor model [27] of V20E275 (Littlefuse, UltraMOV Series) used in the SCASA design predicted that the ON resistances (Var1 and Var2) were between 0.2–1 Ω under transient currents [27,28]. Notably, for transient frequencies, the inductive impedances of two SCASA coupled coils dominated; hence, more the inductive secondary coil (i_2) received only 8% of the surge current, while 92% of the transient current flowed into Var1 through the primary (i_1) coil [29]. More details about the coupled-inductor current division for both transient and 50 Hz RMS conditions were given in our previous publication. In this research, we focus on investigating the voltages induced in primary and secondary coils, as predicted by the following equations. This would further help us understand more about the transformer action shown by the SCASA magnetic core.

When the primary current i_1 and secondary current i_2 propagate through the SCASA core, the opposing voltage barrier induced by the primary coil is determined by the rate of change of the respective currents and the self-/mutual inductances of the primary coil. Hence, by using Equations (11)–(13), the primary induced voltage v_p is written in the following form:

$$v_p = [\Lambda_m + \tfrac{\Lambda_\sigma}{2}] {N_1}^2 \frac{di_1}{dt} + \Lambda_m N_1 N_2 \frac{di_2}{dt} \tag{14}$$

Similarly, the secondary induced voltage v_s can be expressed as:

$$v_s = [\Lambda_m + \tfrac{\Lambda_\sigma}{2}] {N_2}^2 \frac{di_2}{dt} + \Lambda_m N_1 N_2 \frac{di_1}{dt} \tag{15}$$

Since the SCASA transformer's configuration leads to a more inductive secondary coil with $N_2 = 28$ turns (thus, a greater self-inductance: $L_s = 60$ μH) compared to the primary with $N_1 = 6$ turns (self-inductance: $L_p = 3.8$ μH), $v_s > v_p$ during the transient current's propagation through the coupled inductor. Therefore, an inductive voltage (negative) release given by $v_s - v_p$ is demonstrated by the SCASA core immediately after the surge propagation. Furthermore, it can be proven that the energy storage capacity of the SCASA coupled inductor (for different magnetic cores) is indicated by this voltage difference—$v_s - v_p$. Our next aim is to derive an expression $v_s - v_p$; subtracting (14) from (15),

$$v_s - v_p = \Lambda_m + \tfrac{\Lambda_\sigma}{2} [{N_2}^2 \frac{di_2}{dt} - {N_1}^2 \frac{di_1}{dt}] + \Lambda_m N_1 N_2 [\frac{di_1}{dt} - \frac{di_2}{dt}] \tag{16}$$

By using the magnetizing and leakage permeances extracted from the industry (Magnetics Inc., Pittsburgh, PA, USA) and the specifications of the Kool μu powdered toroid ($\Lambda_m = 61 \pm 8\%$ nH/turn^2, $\Lambda_\sigma = 42 \pm 8\%$ nH/turn^2), the magnitude of $v_s - v_p$ can be evaluated for SCASA windings with $N_2 = 28$ and $N_1 = 6$, as described below. In addition,

considering the 8/20 µs 3 kA surge current waveform (Figure 3) and a 92:8% current division in the primary and secondary coils, we can approximate $di_1 = 2760$ A (92% of 3 kA) and $di_2 = 240$ A (8% of 3 kA). Based on the 8/20 µs current wave shape illustrated in Figure 3c, dt can be approximated to 10 µs (time difference between the peak current and zero current). Substituting these values into (16), we get:

$$v_s - v_p = 61 \times 10^{-9} + \frac{42\times10^{-9}}{2}[28^2 \frac{240}{10 \times 10^{-6}} - 6^2 \frac{2760}{10 \times 10^{-6}}] + 61 \times 10^{-9} \times 6 \times 28[\frac{2760}{10 \times 10^{-6}} - \frac{240}{10 \times 10^{-6}}] \quad (17)$$

$$\approx 3314\,\text{V}$$

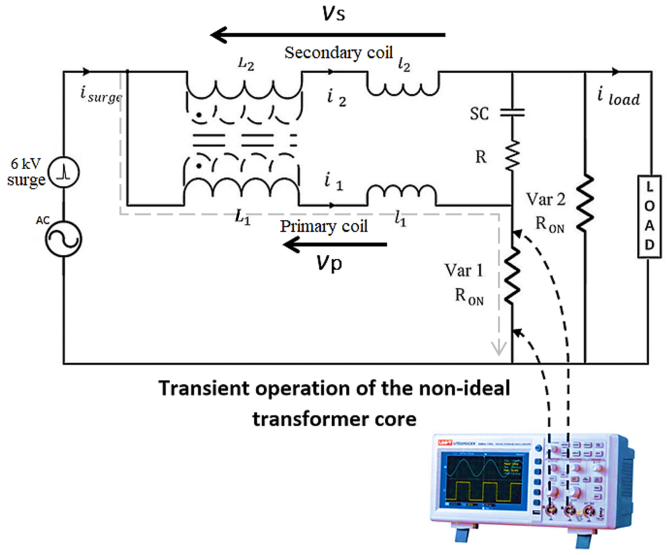

Figure 10. Transient operation of the SCASA transformer.

Consistently with the theoretical voltage difference $v_s - v_p$, the individual voltages induced in the SCASA primary and secondary coils can be calculated as $v_p \approx 1060$ and $v_s \approx 4374$ V (according to (14) and (15)). As $v_s - v_p$ results in a negative voltage release (which passes to Var2 via Var1, as shown in Figure 10) after the propagation of a transient, we captured the Var2 voltage waveform under various LSS surge settings to experimentally compare our theoretical predictions for the SCASA inductive release. All oscilloscope waveforms presented in Figure 11 were obtained by an isolated-channel oscilloscope (Tektronix TPS2014) and high-voltage probes (Tektronix P6015A). According to Figure 11a, the negative peak corresponding to a 6 kV, 3 kA combined transient was found to be ∼−1000 V. However, the theoretical magnitude for $v_s - v_p$ was determined as ∼3314 V, showing a discrepancy with the test waveforms. This effect was due to the saturation of the Kool µu powdered core at high-magnitude surge currents. Therefore, in Section 3.5, we present a detailed analysis of the SCASA toroidal flux for a combined transient of 6 kV and 3 kA and suggest optimization methods by using advanced magnetic materials with a greater saturation flux capacity. Our next aim is to study how the secondary–primary voltage ratio v_s:v_p varies for different transient conditions (with a mismatch with the SCASA turn ratio, $N_2 : N_1$) and to further investigate the non-ideal transformer action of the SCASA coupled inductor.

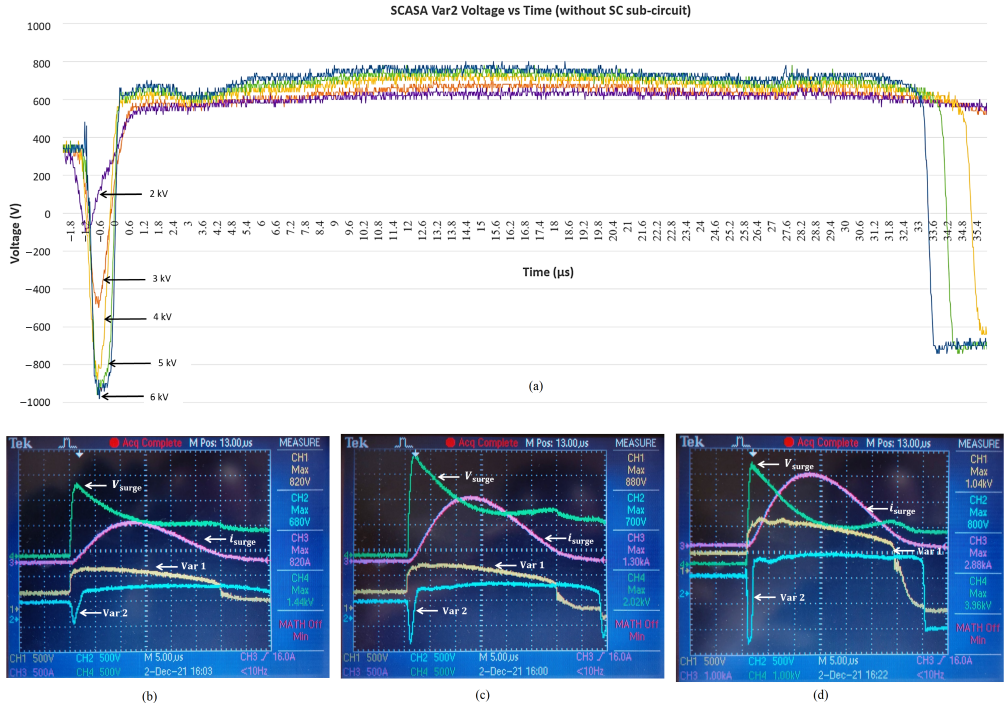

Figure 11. Fluctuation of the Var2 voltage under different surge settings: (**a**) variations in $v_s - v_p$ (negative voltage peak) in the Var2 voltage for 2–6 kV; (**b**) oscilloscope waveform for a 2 kV LSS surge output; (**c**) oscilloscope waveform for a 3 kV LSS surge output; (**d**) oscilloscope waveform for a 6 kV LSS surge output.

3.3. Voltage Ratio and Non-Ideal Transformer Action

As per the theoretical predictions described above (Equations (14) and (15)), the secondary:primary voltage ratio was v_s:v_p = 4.13, and it was consistent with the SCASA turn ratio, $N_2 : N_1$ = 4.6, with a ∼10% deviation. However, this ideal voltage ratio (as in the case of an ideal transformer) deviated considerably according to the experimental and simulated results. To study this non-ideal behavior of the SCASA coupled inductor, we conducted LTSpice simulations under different LSS settings from 1 to 6 kV (Figure 12). In Figure 12a, induced voltages v_s and v_p were found as ∼3.56 kV and ∼1.7 kV, respectively, for the 6 kV surge setting. Therefore, v_s:v_p = 2.1, as verified by the simulated waveform; this significant deviation (compared to the theoretical results) suggests that the SCASA core did not behave as an ideal transformer.

One main factor affecting the transformer action was the type of magnetic material used in the core. The Kool µu powdered toroid consisted of a high concentration of distributed air gaps. This altered the magnetic reluctance ($\Re$) of the core; compared to an ideal transformer, where $\Re = 0$, the Kool µu core had a large reluctance, as calculated below:

$$\Re = \frac{1}{\Lambda_m} = 1.64 \times 10^7 \text{ A.turns/Wb} \tag{18}$$

Another impact of the distributed air gaps in the Kool µu toroid was the reduction effect on the coupling coefficient k; compared to the ideal situation of $k = 1$, the SCASA coupled-inductor windings showed $k = 0.74$ (see Table 3). More information about the SCASA mutual inductances and coupling coefficient variations for different magnetic materials are given below.

In addition, we could identify that the low saturation flux capacity of the Kool µu (10,500 gauss) core was another important factor that affected the ideal transformer action. Due to the high-magnitude surge current (3 kA) propagating through the SCASA windings, the core was saturated, thus lowering the induced voltage ratio v_s:v_p. In Section 3.5, we determine the SCASA toroidal flux for a 3 kA transient and discuss the limitations of

the Kool μu core while introducing several other magnetic materials that are suited for high-performance prototypes.

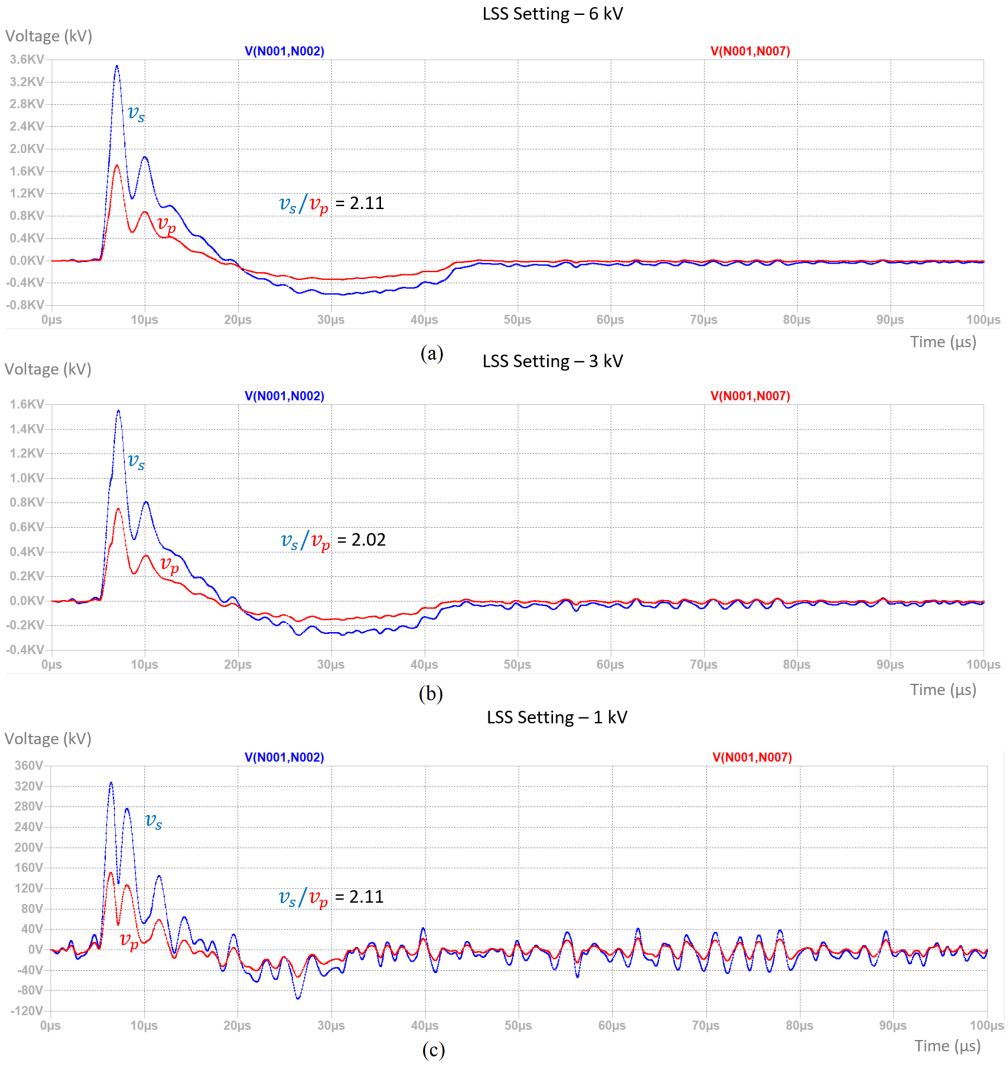

Figure 12. Comparison of the SCASA primary and secondary induced voltages (peak values) under different LSS surge settings: (**a**) LTSpice-simulated waveforms for 6 kV; (**b**) LTSpice-simulated waveforms for 3 kV; (**c**) LTSpice-simulated waveforms for 1 kV.

3.4. LTSpice Simulation Models of SCASA and the Lightning Surge Simulator

In addition to the permeance model of the SCASA magnetic core described above, we conducted a simulation analysis based on an LTSpice circuit model. The model consisted of an LSS-6230 internal generation unit and the details of the SCASA equivalent circuit (non-ideal transformer, MOVs, and SC sub-circuit). Considering the accuracy of our simulation, the X- and Y-type EMI filtering capacitors (C6, C7, and C8), oscilloscope probe parameters, and path impedance (due to parasitic inductances/capacitances) characteristics of connection probes were added to the LTSpice model (see Figures 13 and 14). The LSS wave generation circuit shown in Figure 13 generated standard combinational surge waveforms (1.2/50 μs voltage wave and 8/20 μs current wave), which were then injected into the SCASA circuit. More details about these standard wave shapes were described in Section 1.3.

The equivalent SCASA circuit illustrated in Figure 14 comprised EMI filter capacitors (C6, C7, and C8), oscilloscope probe parameters, and path impedance effects to accurately simulate the transient operation. The magnetizing (L_p, L_s) and leakage (l_1, l_2) inductance

properties of the SCASA coupled-inductor coils were characterized by the coupling coefficients k = 0.74 and k = 0 in the LTSpice model. In addition, the nonlinear behavior of Var1 and Var2 were simulated with the varistor model provided by the Littlefuse cooperation [27]. Transient-mode simulations for the LSS output voltage (V_{surge}), LSS output current (i_{surge}), SCASA primary current (i_1), secondary current (i_2), and voltage clamping of the two SCASA varistors (Var1 and Var2) are demonstrated in Figure 15.

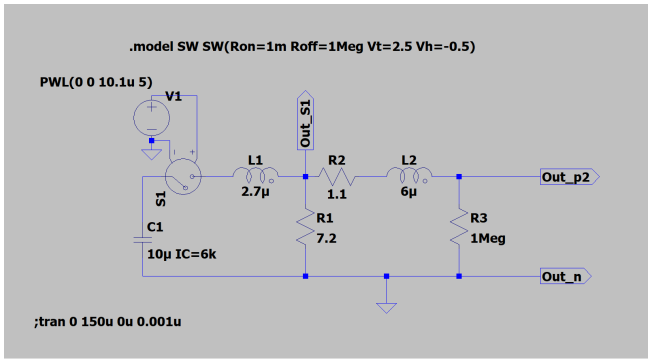

Figure 13. LSS-6230 surge simulator circuit used in the LTSpice simulations.

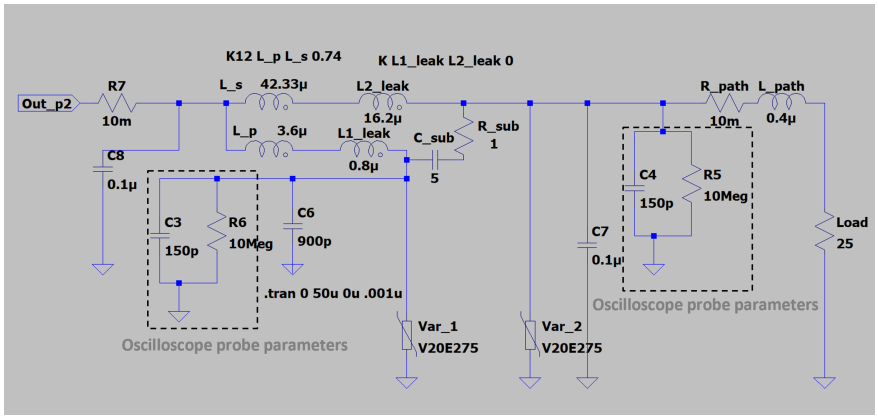

Figure 14. Equivalent circuit of the SCASA topology simulated in LTSpice (including the X- and Y-EMI filtering capacitors (C6, C7, and C8), oscilloscope probe parameters, and path impedance characteristics).

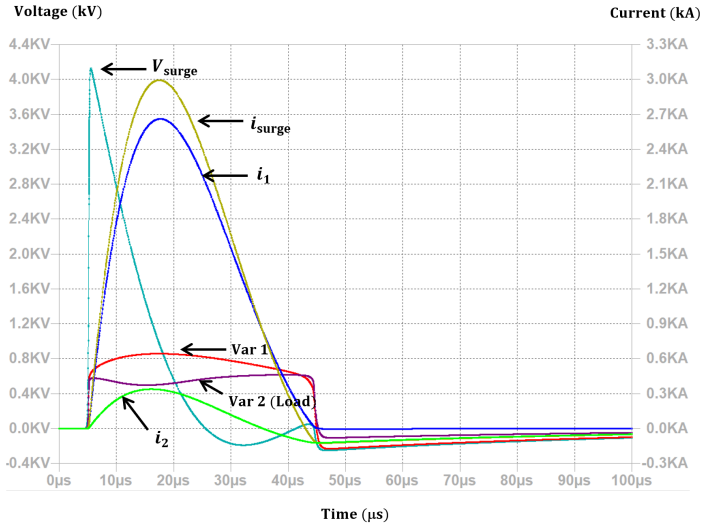

Figure 15. Transient-mode simulations for V_{surge}, i_{surge}, i_1, i_2, and SCASA varistors' clamping variations (Var1 and Var2).

3.5. Toroidal Flux in the SCASA Coupled-Inductor Transformer

Since the induced voltage ratio between the secondary and primary windings of SCASA did not match with the coupled-inductor turn ratio, as described above, our next aim was to investigate the magnetic saturation effects of the core. By evaluating the peak transient flux, our selection of an optimal core material could be justified; this could also prevent SCASA saturation by adopting the right magnetic material. The predictions given below describe how toroidal flux in SCASA was generated for a 6 kV/3 kA transient.

3.6. Toroidal Flux Distribution in SCASA

In Section 2.2, we examined the toroidal magnetization of the SCASA coupled inductor with reference to the Kool μu hysteresis behavior. Here, we expand that theory by deriving a formula (based on Ampere's law) to determine the magnetic flux density $\vec{B}$ induced due to a 3 kA surge current. By applying Ampere's law to a toroid with N turns,

$$\oint_L \vec{B} \cdot \vec{dl} = \sum \mu_c I_{en} \tag{19}$$

Note: $\sum I_{en} = NI$ and $\vec{B}$ = the magnetic flux density due to the surge current I passing through N core windings. As $\vec{B}$ remains steady across the toroidal cross-section, by using core permeability $\mu_c = \mu_r \mu_\circ$, we get

$$B \oint_L dl = \mu_r \mu_\circ NI \tag{20}$$

Note: μ_r = the relative permeability and L = the toroidal circular length (magnetic path length) with radius r. Substituting the integral $\oint_L dl = 2\pi r$ into Equation (20),

$$B = \frac{\mu_r \mu_\circ NI}{2\pi r} \tag{21}$$

Under transient operation, it can be tested that 90% of the surge current I_{surge} propagates through the primary SCASA coil due its low impedance (five turns). Furthermore, the Kool μu (0077071A7, $\mu_r = 60$) powdered iron toroid has a circular length of 81.4 mm ($2\pi r$) [19]. Substituting these into (21), the maximum flux density $B_{\max}$ across the SCASA toroid can be determined for a 3 kA transient as:

$$B_{\max} = \frac{60 \times 4\pi \times 10^{-7} \times 5 \times 0.9 \times 3000}{81.4 \times 10^{-3}}$$

$$B_{\max} \approx 12.5\,\text{T}$$

Given the dynamic nature of rapidly changing transients described in the IEEE 8/20 μs current standard ($I(t) = A_I I_p t^3 e^{-t/\tau}$), we can observe rapid changes in magnetic flux density during SCASA magnetization, as displayed in Figure 16. Note: The graph is based on the assumption that only 90% of the transient current is flowing to the primary coil. The theoretical plot in Figure 16 was drawn in MATLAB according to (22), which was derived from (21).

$$B(t) = \frac{\mu_r \mu_\circ N \left[A_I I_p t^3 e^{-t/\tau} \right]}{2\pi r} \tag{22}$$

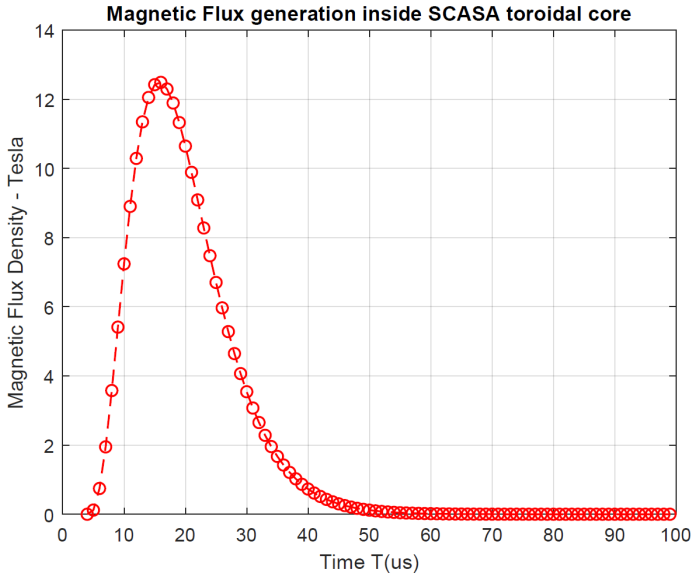

Figure 16. Magnetic flux variation in the SCASA toroidal transformer under a 3 kA transient.

Due to the instantaneous variations in surge transients under 100 µs, the magnetic flux can be appropriately estimated by evaluating the average magnitude of a transient. By integrating over the time interval $T = 100$ µs, the following expression can be established for the transient average I_{avg} as follows:

$$I_{\text{avg}} = \frac{1}{T}\int_0^T A_I I_p t^3 e^{-t/\tau}\, dt \tag{23}$$

By incorporating the IEEE-Std-C62.45-2002 constants $A_I = 0.01243$ µs^{-3}, $\tau = 3.911$ µs, when $I_p = 90\%\ I_{\text{surge}} = 2700$ A, the integral above can be estimated in MATLAB as:

$$I_{\text{avg}} \approx 470 \text{ A}$$

Based on the I_{avg} current, the average magnetic flux density through the SCASA toroid can be determined:

$$B_{\text{avg}} = \frac{\mu_r \mu_\circ N I_{\text{avg}}}{2\pi r} = \frac{60 \times 4\pi \times 10^{-7} \times 5 \times 470}{81.4 \times 10^{-3}} \tag{24}$$

$$B_{\text{avg}} = 2.18 \text{ T}$$

$$B_{\text{avg}} = 21{,}800 \text{ gauss}$$

This is an important finding for our core selection process, as SCASA SPD prototypes are designed with toroids that have similar saturation levels. Details about the magnetic characteristics of different powdered-iron and ferrite samples adopted in SCASA testing are given in the next section.

4. Circuit Modifications and Design Optimizations of SCASA

In this section, we first elucidate how the SCASA topology was modified by using the same Kool µu powdered core as in the original design. Secondly, we discuss the details of advanced prototypes based on X-Flux toroids, High-Flux toroids, and various air-gapped ferrites, which were useful in achieving the best surge absorption for the SCASA protector.

4.1. Addition of a Third Winding to the Magnetic Core

In Section 2.3, we described the importance of storing and leaking transient-related magnetic flux to improve the surge endurance of the SCASA surge protector. Thus, to enhance the flux storage, we first experimented with adding a third coil to the toroidal core of the SCASA design. Figure 17 depicts the topological change made to the base circuit with another supercapacitor (SC) sub-circuit (C_2 and R_2) connected to a third coil wound at N_3 turns. The key idea here was to absorb part of the surge flux flowing through the toroidal core as the SCASA non-ideal transformer became active under the transient mode. The second SC sub-circuit (R_2 and C_2) coupled with the third winding facilitated the dissipation of that absorbed flux in terms of heat. Under 230 V AC operation, when the varistor (MOV) was not fired, the primary coil (N_1 turns) current i_1 was negligible. Therefore, the AC power flow to the load side primarily happened through the secondary coil, which had N_2 turns. More details about AC operation can be found in [29]. Prior to transient-based experiments with this new topology, we first investigated the impact of the third winding on the AC power flow due to the reflected impedance of the coil. The theoretical description presented below quantifies the extra impedance effect due to R_2 and C_2.

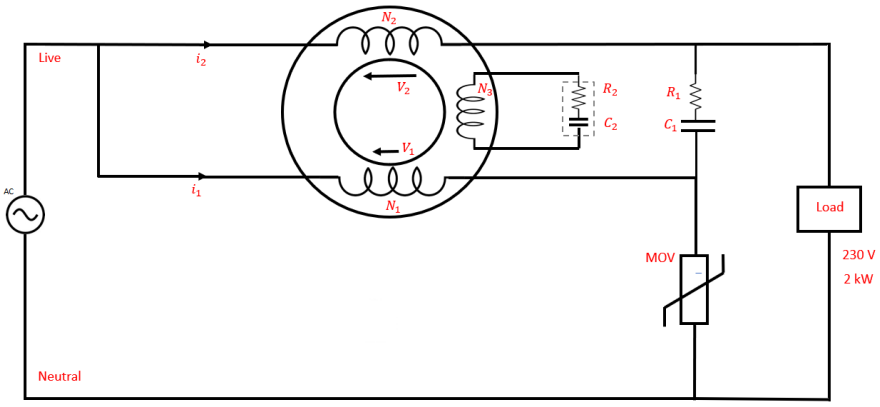

Figure 17. Topological change made to SCASA circuit with the addition of a third winding.

By defining the coefficients α, β, and γ for the respective turn ratios of the primary, secondary, and tertiary windings, we get:

$$\alpha = \frac{N_2}{N_1} \quad \beta = \frac{N_3}{N_1} \quad \text{and} \quad \gamma = \frac{N_3}{N_2} \tag{25}$$

Since the current through the primary winding i_1 is negligible and the secondary current i_2 corresponds to the major power flow, we consider the impact of the tertiary–secondary turn ratio (γ) in our analysis.

The total impedance Z_3 due to R_2 and C_2 placed at the tertiary winding can be written as:

$$Z_3 = R_2 + \frac{1}{j\omega C_2} \tag{26}$$

where ω is 2π times the line frequency of 50 Hz under 230 V AC. By using Equations (25) and (26), the reflected impedance Z_3' onto secondary winding can be expressed by dividing Z_3 by the turn ratio squared:

$$Z_3' = \frac{Z_3}{\gamma^2} = \frac{Z_3}{[N_3/N_2]^2} \tag{27}$$

where γ is the definition of the tertiary–secondary turn ratio. In addition, the 2000 W load device shown in Figure 17 has an equivalent ohmic resistance R_L,

$$R_L = \frac{(230\,\text{V})^2}{2000\,\text{W}} = 26.5\,\Omega$$

Considering R_L and the reflected impedance Z_3', we can evaluate the new RMS current i_2' flowing through the loop between live and neutral as:

$$i_2' = \frac{230\,\text{V}}{26.5\,\Omega + \frac{Z_3}{\gamma^2}\,\Omega} \tag{28}$$

Since the SC impedance ($\frac{1}{j\times 2\pi\times 50\times 5}$) for a 5 F supercapacitor at 50 Hz is fairly small, and when a 10 Ω high-power resistor is used for R_2, i_2' can be simplified as:

$$i_2' = \frac{230\,\text{V}}{26.5\,\Omega + \frac{10}{\gamma^2}\,\Omega}$$

Under these circuit conditions, the new electrical power P' delivered to the load device is determined by using i_2',

$$P' = \left[\frac{230\,\text{V}}{26.5\,\Omega + \frac{10}{\gamma^2}\,\Omega}\right]^2 \times 26.5\,\Omega \tag{29}$$

Using (29), it is possible to evaluate P' under different turn ratios ($\gamma = \frac{N_3}{N_2}$). This gives a satisfactory indication of the appropriate turn ratio to be implemented.

$$\gamma = 2 \rightarrow P' = 1667\,\text{W}$$

$$\gamma = 4 \rightarrow P' = 1906\,\text{W}$$

$$\gamma = 6 \rightarrow P' = 1955\,\text{W}$$

Considering the experimental feasibility and the practicality of the number of turns that can be wound around the Kool μu (0077071A7) powdered-iron toroid, we selected the $\gamma = 4$ condition, where the third coil had 112 turns $(N_3 = 112)$ compared to the 28 turns $(N_2 = 28)$ of the secondary. Furthermore, the active power flow for this condition was 1906 W, and it was not a considerable reduction from the desired 2000 W rated power. As we changed the 10 Ω high-power resistor (R_2) connected to the tertiary winding to much smaller values (1 Ω, 2 Ω, 0.5 Ω, etc.) during the experiments, the impact of the impedance on the AC mains flow became insignificant.

Motivated by the initial investigation of this third coil modification made to the SCASA topology, our next aim was to study its impact under transient operation. Figure 18 demonstrates the experimental setup used to record test results.

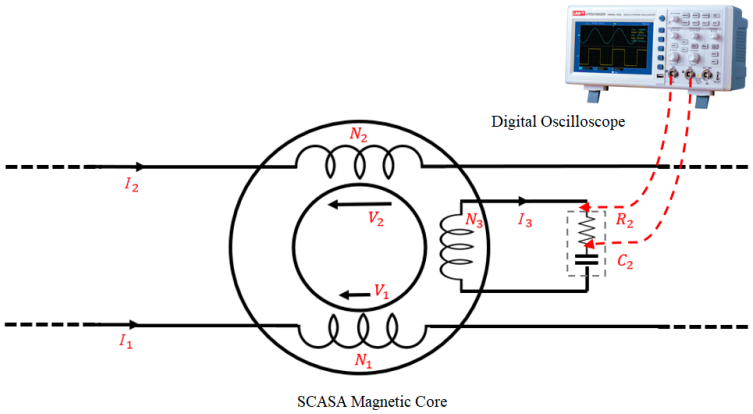

Figure 18. Measurement system for third-coil-based modification made to SCASA (transient mode).

When estimating the energy dissipation across the third coil resistor R_2, we connected a digital oscilloscope (Tektronix TPS2014) to measure the voltage variation across R_2. As the SCASA magnetic core came into transformer action due to transient currents I_1 and I_2, the induced magnetic flux circulates around the toroidal core, resulting in a voltage induction across the third winding. Since the 5 F supercapacitor (C_2) developed a millivolt-order voltage due to its extremely small ESR, the full voltage drop occurred across R_2. Therefore, our measurement system shown in Figure 18 yielded accurate information about the induced voltage and current I_3 through the third coil. This led us to evaluate the heat energy dissipation across R_2 under transient operation (we assumed that the third-coil-induced current I_3 took the standard 8/20 µs wave shape and that the peak energy dissipation occurred at 10 µs). Table 2 summarizes the peak voltages, currents, and corresponding peak energy dissipations for different high-power resistors (varying R_2) placed at the third winding.

Table 2. Comparison of the peak voltages, currents, and peak energy dissipations for different high-power resistors placed at the third winding of SCASA.

Applied Surge (kV)	LSS Surge Current (kA)	Resistance in the Third Coil: $R_2(\Omega)$	V-Peak Across Single-R (V)	I-Peak in the Third Coil (A)	Energy Dissipation $I_3^2R_2.t$ (J) $t \sim 10$ µs
6.0	3.0	1	440 V	440	1.936 J
6.0	3.0	2 (1 × 2)	320 V	320	2.048 J
6.0	3.0	10	1200 V	120	1.44 J
6.0	3.0	100	2000 V	20	0.4 J
6.0	3.0	3 (1 × 3)	220 V	220	1.45 J
6.0	3.0	0.5 (1 ÷ 2)	212 V	424	∼0.9 J

The peak energy estimation presented in Table 2 was carried out when the SCASA circuit was subjected to standard 6 kV/3 kA combinational surge waveforms. Notably, this topological alteration made to the original SCASA core did not significantly improve the surge energy dissipation. However, according to Table 2, it was possible to identify that a maximum energy dissipation ∼2 J could be achieved when two 1 Ω resistors were placed in series (2 Ω) across the third winding. In all other trials with various high-power resistor combinations, serious surge reductions were not achieved. Compared to the ∼81 J energy of an incoming surge, the heat dissipations shown in Table 2 are fairly insignificant. Therefore, we explore alternative optimization methods in the next section.

4.2. Magnetic Properties of the Kool µu, High-Flux, X-Flux, and Other Ferrite Cores

When designing SCASA prototypes for optimal surge absorption, we based our core selection on various powered-iron and ferrite magnetic samples. In Figure 19, the charac-

teristics of three powdered-iron toroids (Kool μu, High-Flux, and X-Flux) and W, J, and R ferrite cores are compared. Our selection criteria for the SCASA prototype components was dependent on three fundamental core properties: permeability, saturation flux, and magnetic permeance. In Section 3, we described the importance of permeance (Λ_m) in theorizing a model for the SCASA coupled-inductor transformer, and we explained how permeance relates to core reluctance ($\Re = 1/\Lambda_m$) when predicting the non-ideal operation of the transformer.

As per the specifications from Magnetics Inc. [19], all three powdered-iron cores revealed reduced permeabilities between 26 and 60 due to the distributed air gaps inside the cores. Consistently with the permeability patterns (as described by (5)), even the permeance values (also known as the inductance factor A_L) of these core samples lay within 28–61 nH/turn^2. Having reduced permeance (and permeability) is suitable for surge protection applications, as distributed air gaps are superior in storing sure energy compared to pure ferrite materials. Therefore, it was predicted that the X-Flux toroid was the best-suited powdered-iron material for the SCASA application. This prediction was further justified by the high saturation level (16,000 gauss) of X-Flux. A similar effect was seen for the two ferrite toroids, where μ_r was equal to 50 and 25 (Λ_m = 67 and 34 nH/turn^2) for the single- and double-gapped cores, respectively. High-permeability (5000–10,000) ungapped ferrites that had very narrow hysteresis behavior were saturated quickly at low magnetic flux; hence, they possessed limited transient energy storage. Therefore, we eliminated the usage of pure J and W ferrites for SCASA optimization. With the goal of substantiating our preliminary predictions, we present the inductance properties of all powdered-iron- and ferrite-based transformers next.

4.3. Inductance Properties of Various Powdered-Iron and Air-Gapped Coupled-Inductor Designs

The essential inductance properties of SCASA, such as the primary/secondary self inductances L_p/L_s, mutual inductance M, and transformer coupling coefficient k, are compared in Table 3 for different prototypes. Out of the three powdered-iron designs, the X-Flux transformer exhibited the weakest magnetic coupling with M = 7.5 and k = 0.56, whereas the presently commercialized SCASA (Kool μu) revealed M = 9.8 and k = 0.74. Consistently with the observations seen in Figure 19, a high concentration of distributed air gaps in X-Flux resulted in an elevation of the leakage flux, thus decreasing the coupling coefficient k. This is a positive aspect for designing surge protectors, as we aim to increase the lossiness of the core by leaking a greater level of surge-induced magnetic flux.

Magnetics Part No.	Material	Relative Permeability (μ_r)	Saturation Flux Density $\vec{B}_{max}$ (gauss)	Permeance Coefficient (Λ_m) (Inductance factor - A_L) ($nH/turn^2$)	Core Reluctance ($\Re$) $\Re = {}^{1}/_{\Lambda_m}$ (ampere-turns per Weber)
0077071A7	Kool μu 	60	10,500	61	1.64×10^7
058071A2-4	High Flux 	60	15,000	61	1.64×10^7
078550A7	X Flux 	26	16,000	28	3.57×10^7
VJ42206TC	J Ferrite	5000	4300	3020	3.31×10^5
0J43515A120 (Air-gapped)	J Ferrite	5000	4300	120	8.33×10^6
ZW43615TC	W Ferrite 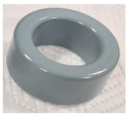	10,000	3900	13,400	7.46×10^4
ZW43615TC (single-gapped)	W Ferrite 	50	3900	67	1.52×10^7
ZW43615TC (Double-gapped)	W Ferrite 	25	3900	34	2.94×10^7
R43521A125 (Gapped EER)	R Ferrite 	105	4700	125	8.0×10^6

Figure 19. Magnetic properties comparison of different powdered-iron and ferrite core types used for SCASA prototypes.

With regard to the ferrite coupled-inductor designs, it could be seen that the gapped EER core, which had a coupling coefficient of $k = 0.74$, had a remarkable similarity to the original Kool μu design. In contrast, the pure ferrite toroid (μ_r = 10,000, $k = 0.99$) was found to be ineffective in SCASA due to its strong magnetic coupling and weak leakage flux. Other toroidal gapped ferrites (single/double gapped) composed of manually inserted air gaps yielded promising inductance values, as shown in Table 3; however, due to their high

cost and inconvenience of production, low-cost mass-produced EER cores were preferred. The test measurements discussed so far provide a good understanding of the suitability of different cores for SCASA transient suppression; LSS surge immunity tests will be presented next.

Table 3. Comparison of the inductance properties of various powdered-iron and ferrite cores used for SCASA prototypes.

Core Property	L_p (μH)	L_s (μH)	N_1	N_2	M (μH)	k
Kool μu Toroid (0077071A7) μ_r = 60	3.4	57	6	28	9.8	0.74
High Flux Toroid (058071A2) μ_r = 60	3.3	58	6	28	8.6	0.61
X Flux Toroid (078550A7) μ_r = 26	3	59.8	8	44	7.5	0.56
Ferrite Toroid (ZW43615TC) μ_r = 10,000	312	11,200	6	28	1870	0.99
Single-gapped Ferrite (ZW43615TC) μ_r = 50	13	170	6	28	42	0.82
Double-gapped Ferrite (ZW43615TC) μ_r = 25	6	65	6	28	12	0.58
Gapped EER Ferrite (R43521A125) μ_r = 105	7.7	236	6	34	31.5	0.74

4.4. Experimental Setup for Surge Immunity Tests

In Section 1.3, we presented details about the standard combinational waveforms (1.2/50 µs open-circuit voltage wave and 8/20 µs current wave) used for SPD testing. In a high-voltage laboratory encased similarly to a Faraday cage, where electromagnetic radiation was shielded, Lightning Surge Simulators (LSS-6230 and LSS-F03) were used to generate combined transients of a magnitude of 6 kV/3 kA. The device-under-test (DUT) SCASA coupled inductor was connected to 230 V mains via LSS-6230, as shown in Figure 20.

When combinational surges were injected into the mains flow, the SCASA magnetic core absorbed the surge energy, while both MOVs (Var1 and Var2) provided clamping (by dissipating excess energy) to protect the load. In order to capture clamped voltages, we used a digital oscilloscope with a 100 MHz bandwidth and 1 GS/s sample rate (Tektronix-TPS2014), and it had four isolated channels that were suitable for high-voltage floating measurements. These oscilloscope channels were isolated from each other, as well as from Earth ground, thus providing accurate differential measurements of MOV clamping with the Tektronix P6015A high-voltage probes connected to varistor terminals (Figure 20). Moreover, two of the isolated channels were separately connected to LSS-6230 reference outputs (1000× attenuated) to obtain the surge wave shapes (V_{surge} and i_{surge}) injected into

the DUT line. Next, the usability and energy storage levels of different SCASA prototypes under combinational surge testing will be discussed.

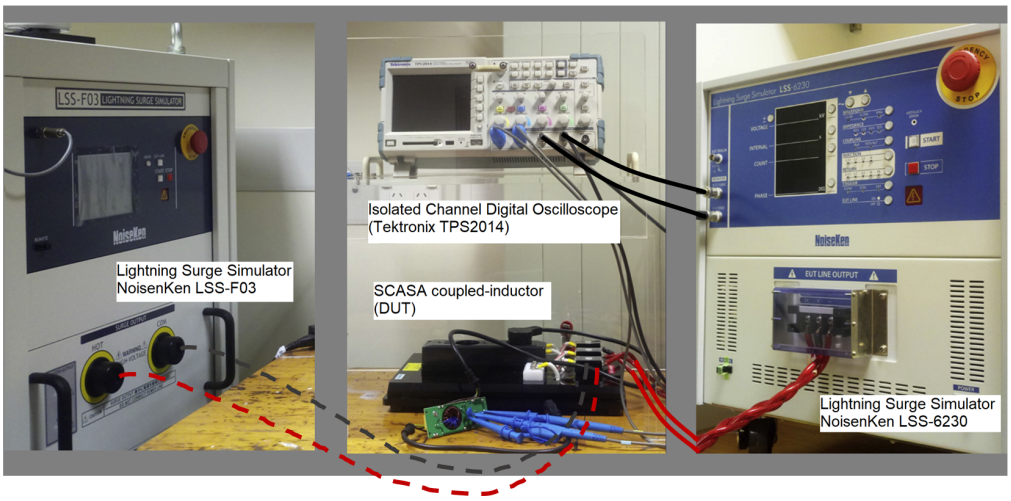

Figure 20. Measurement system for testing the surge absorption of SCASA coupled-inductor designs.

4.5. Performance Comparison and Future Work

In Section 3.2, it was revealed that the transient absorption capabilities of the SCASA coupled-inductor core were indicated by the magnitude of $v_s - v_p$, where v_s is the secondary induced voltage and v_p is the primary induced voltage. Therefore, we first analyzed the relative energy absorption capacities of seven different core types (coupled-inductor designs), as shown in Table 4. All seven prototypes mentioned in Table 4 were subjected to 6 kV/3 kA combinational surge waveforms coupled with 230 V/50 Hz mains, as illustrated in Figure 20. In this research, we mainly used LSS-6230 for surge generation, as the peak surge magnitudes did not exceed 6 kV for SCASA testing. However, the more advanced LSS-F03, which had a 15 kV peak voltage, was used as a reference to analyze combinational wave shapes.

According to Table 4, it can be seen that the X-Flux-based coupled inductor had the best surge absorption out of the three powdered-iron cores, with an inductive voltage release ($v_s - v_p$) of −1160 V. Both the Kool μu and High-Flux powdered-iron designs revealed moderate to low levels of absorption, respectively. Moreover, the four ferrite designs showed contrasting performances under transient surge testing. The high-permeance (Λ_m = 13,400 nH/turn^2) pure ferrite had poor energy storage capabilities, whereas all gapped ferrites indicated elevated surge-absorbing capacities. Out of the two manually gapped ferrite toroids, the double-gapped core (Λ_m = 34 nH/turn^2) stored the most surge flux, while the single-gapped core (Λ_m = 67 nH/turn^2) showed similar characteristics to those of the Kool μu design, with a moderate level of absorption. Notably, the centre-gapped EER ferrite signified the greatest surge-absorbing capabilities out of all seven coupled-inductor designs. The EER core, which had a permeance of 125 nH/turn^2, also revealed an inductive release of −1260 V, as highlighted in Table 4.

As previously described in Section 2, a significant share of surge energy was dissipated in two SCASA varistors (Var1 and Var2). Having a greater absorption in the coupled-inductor core reduces the heat stress on the two varistors, thus minimizing the clamping voltage across Var1 and Var2. Therefore, a core that absorbs more transient energy safeguards the critical load effectively with a low voltage clamping. Of the two varistors, Var2 is of extreme importance to our study, as Var2 directly connects to the load circuit. A good agreement of this effect can be seen in Table 4, as both the X-Flux and EER-type prototypes yielded the best SCASA performance for the load side. Consistently with the pattern of high surge absorption described above, the X-Flux powdered core displayed a low clamping of 840 V (∼10% reduction from the original Kool μu design) for

Var2, whereas the best clamping voltage of 740 V (∼20% reduction) was revealed by the air-gapped EER core.

Table 4. Comparison of the energy storage capabilities and clamping voltage reductions for different powdered-iron and ferrite-based SCASA prototypes.

Magnetic Core Type and Permeance (Λ_m)	Magnitude of ($v_s - v_p$)	Energy Storage Capability	Clamping Voltage (Varistor 1)	Clamping Voltage (Varistor 2)	Usability in SCASA Max. Surge Endurance (UL 1449)	Approximate Production Cost
Kool μu Λ_m= 61 nH/turn^2	−860 V	Moderate	944 V	928 V	Usable (Failure after 150 surges)	x
High Flux (058071A2) Λ_m= 61 nH/turn^2	−100 V	Low	948 V	920 V	Limited (Failure after 100 surges)	4x
X Flux (078550A7) Λ_m= 28 nH/turn^2	−1160 V	High	942 V	840 V (∼10% reduction)	Highly Usable (Failure after 250 surges)	1.2x
Ferrite Toroid (ZW43615TC) Λ_m= 13,400 nH/turn^2	−60 V	Low	980 V	944 V	Not Usable	0.9x
Single-gapped Ferrite (ZW43615TC) Λ_m= 67 nH/turn^2	−1080 V	Moderate	960 V	860 V	Usable (Failure after 150 surges)	∼1.1x
Double-gapped Ferrite (ZW43615TC) Λ_m= 34 nH/turn^2	−1180 V	High	920 V	800 V	Highly Usable (Failure after 250 surges)	∼1.2x
Gapped EER Ferrite (R43521A125) Λ_m= 125 nH/turn^2	−1260 V	High	920 V	740 V (∼20% reduction)	Highly Usable (Failure after 250 surges)	∼0.6x

To consolidate the performance observations demonstrated by all coupled-inductor designs, we subjected them to UL-1449 surge endurance tests specified by Underwriters' Laboratories [30]. According to the UL-1449 test protocol, 6 kV/3 kA combinational waveforms were consecutively injected into the SCASA prototypes with particular time gaps in between; more details about the consecutive surge count and time gaps are given in [30]. Out of all prototypes summarized in Table 4, the EER ferrite and X-Flux powdered-iron toroid withstood the maximum numbers of consecutive surges, where the failure of Var2 was seen after 250 transient surges, as per the UL standard. A similar surge endurance was shown by the double-gapped ferrite, but due to experimental difficulties, we ignored the manual gapping of toroids. The presently commercialized coupled inductor based on the Kool μu toroid also revealed a moderate yet substantial surge-withstanding capability for up to 150 consecutive pulses. Another important attribute that is relevant to our core selection is the manufacturing cost. Due to commercial price constraints, the SCASA surge protector can be mass-produced by reducing the cost of its coupled inductor. Notably, it was found that the EER ferrite design, which had the best surge absorption/endurance, also indicatd a ∼40% cost reduction compared to the Kool μu design.

5. Conclusions

Supercapacitor-assisted techniques are a unique set of circuit topologies designed to fulfill power conversion and protection tasks by circumventing the energy losses that are normally associated with RC-based circuits. With a capacitance that is a million times larger than that of the electrolytic type, supercapacitors have shown a remarkable surge

endurance, as discovered by the University of Waikato Power Electronics Group. This research examined the patented SCASA surge protector based on the novel use of SCs' surge-withstanding capabilities and investigated ways to optimize the present design based on improvements made to the circuit's magnetic components.

To envisage the SCASA operation, we first identified coupled-inductor transformer action under transient conditions. In predicting voltage induction under 50 Hz AC and transients, a permeance model was used. Our model highlighted the non-ideal characteristics of the coupled inductor, such as its leakage and magnetizing inductances, and it provided theoretical predictions based on the permeance coefficients extracted from industrial specifications. The SCASA inductances were measured over a range of kilohertz-order frequencies to confirm the accuracy of the modeling work.

In addition, this study elucidated the design details of different coupled-inductor topologies for improved transient absorption. According to surge tests carried out by using SCASA prototypes, it was revealed that:

- The commercially available X-Flux powdered-iron toroid and air-gapped EER ferrite yielded exceptional performance with ∼10% and ∼20% lower load–voltage clamping compared to the Kool μu design.
- The X-Flux powdered core and gapped EER demonstrated a remarkable surge endurance, withstanding over 250 consecutive surges as per the UL-1449 standard.
- The air-gapped EER ferrite had a minimized inductance tolerance and ∼40% reduction in the manufacturing cost.

The experimental procedures presented in this research are compliant with the IEEE C62.41 and IEC 61000-4-5 standards. Standard surge waveforms were generated by using a lightning surge simulator (Noiseken LSS-6230) coupled with 230 V, 50 Hz utility mains.

The permeance model adopted when theorizing the core inductance properties indicated that the ideal permeance range for the SCASA coupled inductor is within $28 < \Lambda_m < 125$ nH/Turn^2, thus confirming the suitability of powdered and gapped core designs. This paper also covered the details of three-winding design optimizations, the SCASA voltage action, and LTSpice simulations under transient conditions. In future research work, surge energy distribution among various SCASA circuit components will be investigated. Transient energy estimations will be evaluated based on a Laplace transform analysis of the SCASA circuit model.

Author Contributions: Conceptualization, S.S.T.; methodology, S.S.T.; software, S.S.T.; validation, S.S.T.; formal analysis, S.S.T.; investigation, S.S.T.; resources, S.S.T.; data curation, S.S.T.; writing—original draft preparation, S.S.T.; writing—review and editing, S.S.T.; supervision, N.K.; supervision, D.A.S.-R. All authors have read and agreed to the published version of the manuscript.

Funding: This research received no external funding.

Institutional Review Board Statement: Not applicable.

Informed Consent Statement: Not applicable.

Acknowledgments: The authors would like to thank Bradley M. Yourish of Magnetics Inc. for providing the magnetic samples required for the SCASA coupled-inductor designs. We kindly appreciate his cooperation in this regard.

Conflicts of Interest: The authors declare no conflict of interest.

Abbreviations

The following abbreviations are used in this manuscript:

AC	Alternating Current
DUT	Device Under Test
EC	Electrolytic Capacitor
EDLC	Electric Double-Layer Capacitor
LSS	Lightning Surge Simulator
NLD	Nonlinear Device
GDT	Gas Discharge Tube
BBD	Bidirectional Break-Over Diode
MOV	Metal Oxide Varistor
RMS	Root Mean Square
SC	Supercapacitor
SCASA	Supercapacitor-Assisted Surge Absorber
SPD	Surge Protector Device
SMART TViQ	Commercial Implementation of the SCASA Technique
THY	Thyristor
Var1 and Var2	Varistor 1 and Varistor 2
ITRS	International Technology Roadmap for Semiconductors

References

1. *IEC 60038:2009*; IEC Standard Voltages. International Electrotechnical Commission: Geneva, Switzerland, 2009–2022.
2. Chudnovsky, B.H. *Electrical Power Transmission and Distribution: Aging and Life Extension Techniques*; CRC Press: Boca Raton, FL, USA, 2020.
3. Papailiou, K.O. *Springer Handbook of Power Systems*; Springer: Singapore, 2021.
4. Holland, S.S.; Richie, J.E.; Strangeway, R.A. *Electromagnetics and Transmission Lines: Essentials for Electrical Engineering*; Wiley: Hoboken, NJ, USA, 2022.
5. *IEEE Std C62.62-2018*; IEEE Standard Test Specifcations for Surge-Protective Devices (SPDs) for Use on the Load Side of the Service Equipment in Low-Voltage (1000 V and Less) AC Power Circuits. 2018; pp. 1–61. Available online: https://ieeexplore.ieee.org/document/8430667 (accessed on 16 October 2022).
6. Kularatna, N.; Steyn-Ross, A.; Fernando, J.; James, S. *Design of Transient Protection Systems: Including Supercapacitor Based Design Approaches for Surge Protectors*; Elsevier: Amsterdam, The Netherlands, 2018.
7. *IEEE Std C62.45-2002*; IEEE Recommended Practice on Surge Testing for Equipment Connected to Low-Voltage (1000 V and Less) AC Power Circuits. (Revision of IEEE Std C62.45-1992), pp. 1–85. Available online: https://ieeexplore.ieee.org/document/1196925 (accessed on 16 October 2022).
8. NoiseKen Laboratories. *Lightning Surge Simulator LSS-6230A*; Technical Report; NoiseKen Laboratory Co., Ltd.: 2020. Available online: http://www.noiseken.com/modules/products/index.php?contentid=211 (accessed on 16 October 2022).
9. NoiseKen Laboratories. *Lightning Surge Simulator LSS-F03 Series*; Technical Report; NoiseKen Laboratory Co., Ltd.: 2022. Available online: http://www.noiseken.com/modules/products/index.php?contentid=249 (accessed on 16 October 2022).
10. Sharma, A.L.; Gaur, A. *Energy Storage and Conversion Devices: Supercapacitors, Batteries, and Hydroelectric Cells*; CRC Press: Boca Raton, FL, USA, 2021.
11. Raza, W.; Ali, F.; Raza, N.; Luo, Y.; Kim, K.-H.; Yang, J.; Kumar, S.; Mehmood, A.; Kwon, E.E. Recent advancements in supercapacitor technology. *Nano Energy* **2018**, *52*, 441–473. [CrossRef]
12. Thotabaddadurage, S.U.S. Permeance based Modelling, Design and Optimization of Supercapacitor Assisted Surge Absorber (SCASA). Ph.D. Thesis, The University of Waikato, Hamilton, New Zealand, 2021.
13. Fernando, J. Supercapacitor-Assisted Surge Absorber (SCASA) and Supercapacitor Surge Modelling. Ph.D. Thesis, The University of Waikato, Hamilton, New Zealand, 2016.
14. Udayanga, S.T.S.; Kularatna, N.; Steyn-Ross, D.A. Permeance based model for the coupled-inductor utilized in the supercapacitor assisted surge absorber (SCASA) and its experimental validation. In Proceedings of the 2nd IEEE International Conference on Industrial Electronics for Sustainable Energy Systems (IESES), Cagliari, Italy, 20–22 April 2020; pp. 267–272.
15. Fernando, J.; Kularatna, N.; Silva, S.; Thotabaddadurage, S.S. Supercapacitor assisted surge absorber technique: High performance transient surge protectors for consumer electronics. *IEEE Power Electron. Mag.* **2022**, *9*, 48–60. [CrossRef]
16. 'Thor Technologies—STViQ/3 SMART TViQ'. 2022. [Online]. Available online: https://www.thortechnologies.com.au/product/stviq3/ (accessed on 22 April 2022).
17. Magnetics—'Ferrite Core Documents', Maginc.com. 2021. [Online]. Available online: https://www.maginc.com/Design/TechnicalDocuments/Ferrite-Core-Documents (accessed on 10 December 2021).
18. Thotabaddadurage, S.S.; Kularatna, N.; Steyn-Ross, D.A. Importance of Leakage Magnetic Field and Fringing Flux in Surge Protector Design. *IEEE Trans. Ind. Appl.* **2022**. [CrossRef]

19. Magnetics Inc. '2021 Magnetics Powder Core Catalogue', Mag-inc.com. 2021. Available online: https://www.maginc.com/Design/Technical-Documents/Powder-Core-Documents (accessed on 26 January 2022).
20. McLyman, C.W.T. *Transformer and Inductor Design Handbook*; CRC Press: Boca Raton, FL, USA, 2017.
21. Silva, S.U.; Kularatna, N.; Steyn-Ross, D.A. Optimization of Supercapacitor Assisted Surge Absorber (SCASA) Technique: A New Approach to Improve Surge Endurance Using Air Gapped Ferrite Cores. *Energies* **2021**, *14*, 4337. [CrossRef]
22. Udayanga, S.T.S.; Kularatna, N.; Steyn-Ross, D.A. Investigating the Impact of Ferrite Magnetic Cores on the Performance of Supercapacitor Assisted Surge Absorber (SCASA) Technique. In Proceedings of the 2019 IEEE 28th International Symposium on Industrial Electronics (ISIE), Vancouver, BC, Canada, 12–14 June 2019; pp. 130–135.
23. Kazimierczuk, M.K. *High-Frequency Magnetic Components*; Wiley: West Sussex, UK 2014.
24. Bossche, A.; Valchev, V. *Inductors and Transformers for Power Electronics*; Taylor & Francis: New York, NY, USA, 2018.
25. Ertan, H.B.; Turowski, J.; Lopez-Fernandez, X.M. *Transformers: Analysis, Design, and Measurement*; CRC Press: Boca Raton, FL, USA, 2017.
26. AN9767.1. *Littelfuse Varistors—Basic Properties, Terminology and Theory*; Technical Report; Littlefuse Co-operation: 1999. Available online: https://www.littelfuse.com/~/media/electronicstechnical/applicationnotes/varistors/littelfusevaristorsbasicproperties/terminologyandtheoryapplicationnote.pdf (accessed on 16 October 2022).
27. Littelfuse Inc. Ultra MOV Varistor Series: Radial Lead Varistors. 2019. Available online: https://www.littelfuse.com/~/media/electronics/datasheets/varistors/littelfusevaristorultramovdatasheet.pdf.pdf (accessed on 28 December 2021).
28. Maytum, M. There's an "R" in "Varistor". 2020. Available online: https://incompliancemag.com/article/theres-an-r-in-varistor/ (accessed on 24 November 2020).
29. Thotabaddadurage, S.U.S.; Kularatna, N.; Steyn-Ross, D.A. Permeance based Design and Analysis of Supercapacitor assisted Surge Absorber for Magnetic Component Selection. *IEEE Trans. Ind. Electron.* **2022**. [CrossRef]
30. UL 1449. *UL Standard for Surge Protective Devices*, 5th ed.; Underwriters Laboratories Inc.: Brooklyn, IL, USA, 2021.